Title

Differential Activity-Dependent Increase in Synaptic Inhibition and Parvalbumin Interneuron Recruitment in Dentate Granule Cells and Semilunar Granule Cells.

Journal

Journal of Neuroscience, 42(6)

ISSN

0270-6474

Authors

Afrasiabi, Milad
Gupta, Akshay
Xu, Huaying
et al.

Publication Date

2022-02-09

DOI

10.1523/jneurosci.1360-21.2021

Peer reviewed

Systems/Circuits

Differential Activity-Dependent Increase in Synaptic Inhibition and Parvalbumin Interneuron Recruitment in Dentate Granule Cells and Semilunar Granule Cells

Milad Afrasiabi,[1] Akshay Gupta,[1,2] Huaying Xu,[3] Bogumila Swietek,[1] and Vijayalakshmi Santhakumar[1,2]

[1]Department of Pharmacology, Physiology and Neuroscience, Rutgers New Jersey Medical School, Newark, New Jersey 07103, [2]Department of Molecular, Cell and Systems Biology, University of California Riverside, Riverside, California 92521, and [3]Department of Statistics, University of California Riverside, Riverside, California 92521

Strong inhibitory synaptic gating of dentate gyrus granule cells (GCs), attributed largely to fast-spiking parvalbumin interneurons (PV-INs), is essential to maintain sparse network activity needed for dentate dependent behaviors. However, the contribution of PV-INs to basal and input-driven sustained synaptic inhibition in GCs and semilunar granule cells (SGCs), a sparse morphologically distinct dentate projection neuron subtype, is currently unknown. In studies conducted in hippocampal slices from mice, we find that although basal IPSCs are more frequent in SGCs and optical activation of PV-INs reliably elicited IPSCs in both GCs and SGCs, optical suppression of PV-INs failed to reduce IPSC frequency in either cell type. Amplitude and kinetics of IPSCs evoked by perforant path (PP) activation were not different between GCs and SGCs. However, the robust increase in sustained polysynaptic IPSCs elicited by paired afferent stimulation was lower in SGCs than in simultaneously recorded GCs. Optical suppression of PV-IN selectively reduced sustained IPSCs in SGCs but not in GCs. These results demonstrate that PV-INs, while contributing minimally to basal synaptic inhibition in both GCs and SGCs in slices, mediate sustained feedback inhibition selectively in SGCs. The temporally selective blunting of activity-driven sustained inhibitory gating of SGCs could support their preferential and persistent recruitment during behavioral tasks.

Key words: **dentate gyrus; feedback inhibition; GABA; parvalbumin; semilunar granule cell**

Significance Statement

Our study identifies that feedback inhibitory regulation of dentate semilunar granule cells (SGCs), a sparse and functionally distinct class of projection neurons, differs from that of the classical projection neurons, GCs. Notably, we demonstrate relatively lower activity-dependent increase in sustained feedback inhibitory synaptic inputs to SGCs when compared with GCs which would facilitate their persistent activity and preferential recruitment as part of memory ensembles. Since dentate GC activity levels during memory processing are heavily shaped by basal and feedback inhibition, the fundamental differences in basal and evoked sustained inhibition between SGCs and GCs characterized here provide a framework to reorganize current understanding of the dentate circuit processing.

Introduction

The hippocampal dentate gyrus is known for its uniquely sparse activity, essential for its function in pattern separation, a process of disambiguating similar inputs into distinct patterns of neural activity and memory representations (Bekinschtein et al., 2013; GoodSmith et al., 2017). The characteristically sparse dentate activity is maintained by the relatively hyperpolarized resting membrane potential and low input resistance of the projection neurons and their powerful inhibitory regulation (Heinemann et al., 1992; Lothman et al., 1992). Dentate inhibition includes sustained tonic/extrasynaptic GABA currents as well as distinct phases of synaptic inhibition, which shape basal and afferent-evoked activity (Stell et al., 2003; Ewell and Jones, 2010). Apart from the classical basal spontaneous synaptic inhibition and afferent evoked feedforward and feedback inhibition, dentate granule cells (GCs) have been proposed to receive "sustained" increase in feedback synaptic inhibition following paired stimulation of perforant path (PP) inputs (Larimer and Strowbridge,

Received June 26, 2021; revised Oct. 12, 2021; accepted Oct. 24, 2021.

Author contributions: V.S. designed research; M.A. and B.S. performed research; M.A., A.G., and H.X. analyzed data; M.A. wrote the first draft of the paper; M.A. edited the paper; V.S. wrote the paper.

This work was supported by National Institutes of Health/National Institute of Neurological Disorders and Stroke Grants R01 NS069861 and R01NS097750 and New Jersey Commission on Brain Injury Research Grants CBIR16IRG017 (to V.S.), CBIR15FEL011 (to M.A.), and CBIR11FEL003 (to A.G.). We thank Dr. Luke Fritzky at the Rutgers Imaging Core for help with imaging, Dr. Archana Proddutur for immunostaining validation of transgenic mouse lines, and Dr. Deepak Subramanian for developing schematics.

The authors declare no competing financial interests.

Correspondence should be addressed to Vijayalakshmi Santhakumar at vijayas@ucr.edu.

https://doi.org/10.1523/JNEUROSCI.1360-21.2021

2010). This sustained feedback inhibition has been suggested as a mechanism for surround inhibition needed to facilitate pattern separation (Larimer and Strowbridge, 2010; Walker et al., 2010). However, the reliability, cell specificity and temporal structure of this sustained feedback inhibition is not known and the identity of inhibitory neurons recruited during this prolonged feedback inhibition has not been examined.

Although dentate GCs have, for long, been considered a structurally and functionally uniform class of projection neurons, detailed morphometric and physiological analysis in rats have revealed a sparse, structurally distinct population of neurons with axonal projections to CA3 described as semilunar granule cells (SGCs) by Ramón y Cajal (1995; Williams et al., 2007; Gupta et al., 2012; Save et al., 2018). Functionally, SGCs have sustained firing in response to paired PP stimulation, which distinguish them from GCs (Larimer and Strowbridge, 2010). While SGCs, characterized by wider dendritic span, have been reported in mice (Save et al., 2018; Erwin et al., 2020), detailed morphometric analysis and functional characterization of SGCs in mice is lacking. Of particular relevance to dentate inhibitory regulation, whether SGCs receive similar early (feedforward or disynaptic feedback) as well as sustained polysynaptic feedback inhibition as GCs or may escape this inhibitory gate is currently unknown. Studies in adolescent rats show that SGCs have higher tonic GABA currents and receive more frequent synaptic inhibitory inputs than GCs (Gupta et al., 2012, 2020). Uniquely, SGCs show reduction in both tonic GABA currents and frequency of synaptic inhibitory inputs after brain injury rather than the increase observed in GCs (Gupta et al., 2012). While these findings suggest different interneuron subtypes may contribute to synaptic inhibition in GCs and SGCs, which class of dentate interneurons underlie this differential control, is not known. Parvalbumin interneurons (PV-INs) are a major class of GABAergic neurons which are classified by expression of the calcium binding protein parvalbumin and their fast, non-adapting firing pattern. PV-INs include the perisomatically projecting basket cells which contribute to feedforward and feedback inhibition of GCs (Kraushaar and Jonas, 2000; Hefft and Jonas, 2005; Ewell and Jones, 2010) and axo-axonic cells which target GC axon-initial segments (Sik et al., 1997; Howard et al., 2005). A single basket cell can project to as many as 10,000 GCs (Freund and Buzsáki, 1996; Santhakumar, 2008) and is an ideal candidate to mediate surround inhibition. However, whether PV-INs innervate SGCs with somata located in the inner molecular layer (IML), outside the dense axon collaterals of PV-positive basket cells has not been tested.

Recent studies have indicated that SGCs may be disproportionately recruited to memory engrams (Erwin et al., 2020) making it important to understand whether inhibitory regulation of SGCs differs from that of GCs. This study was conducted to systematically examine the cell-type-specific differences in distinct phases of synaptic inhibition; basal spontaneous synaptic inhibition, PP evoked, early feedforward, and feedback inhibition as well as sustained feedback inhibition, between the two classes of dentate projection neurons and to determine the contribution of PV-INs to specific phases of inhibition in GCs and SGCs.

Materials and Methods

Animals

All experiments were performed in accordance with IACUC protocols approved by Rutgers-NJMS, Newark, NJ, and the University of California at Riverside, CA and in keeping with the ARRIVE guidelines. The study included male and female wild-type C57BL/6J (WT) or appropriately validated optogenetic mice (four to eight weeks old, The Jackson Laboratory). PV-Cre mice (B6;129P2-Pvalbtm1(cre)Arbr/J; JAX #8069) were crossed with either of the two floxed lines (Chr2-YFP: B6;129S-Gt (ROSA)26Sortm32(CAG-COP4*H134R/EYFP)Hze/J; JAX#12 569 or NpHR3-YFP: Rosa-CAG-LSL-eNpHR3.0-EYFP-WPRE; JAX #14 539) to generate experimental PV-Chr2 and PV-NpHR3 mice. Immunofluorescence labeling for PV and YFP in sections from PV-YFP mice identified that over 80% of PV labeled cells expressed YFP, and all YFP positive cells expressed PV validating the specificity of the PV-Cre transgenic lines. Mice were housed with littermates (four mice per cage) in a 12/12 h light/dark cycle. Food and water were provided *ad libitum*.

Slice physiology

Animals were anesthetized under 3% isoflurane and decapitated. Whole brains were extracted and horizontal brain slices (350 μm) were prepared using Leica VT1000 or VT1200S Vibratomes in ice-cold high sucrose-artificial CSF (aCSF) containing 85 mM NaCl, 75 mM sucrose, 24 mM $NaHCO_3$, 25 mM glucose, 4 mM $MgCl_2$, 2.5 mM KCl, 1.25 mM NaH_2PO_4, and 0.5 mM $CaCl_2$. Slices were bisected and incubated at 32 ± 1°C for a minimum of 30 min in a submerged holding chamber containing recording aCSF and subsequently held at room temperature (RT; 22–23°C). The recording aCSF contained 126 mM NaCl, 2.5 mM KCl, 2 mM $CaCl_2$, 2 mM $MgCl_2$, 1.25 mM NaH_2PO_4, 26 mM $NaHCO_3$, and 10 mM D-glucose. All solutions were saturated with 95% O_2 and 5% CO_2 and maintained at a pH of 7.4 for 2–6 h (Gupta et al., 2012; Yu et al., 2016).

Slices (350 μm) were transferred to a submerged recording chamber and perfused with oxygenated aCSF at 33 ± 1°C. Whole-cell voltage-clamp and current-clamp recordings from GCs, SGCs, and presumed interneurons at the border of the hilus and GC layer (GCL) were performed under IR-DIC visualization with a Nikon Eclipse FN-1 (Nikon Corporation) or Olympus BX50 (Olympus Corporation) microscope, using 40× water-immersion objectives. Recordings were obtained using Molecular Devices Axopatch 200B or MultiClamp 700B amplifiers (Molecular Devices). Data were obtained using glass microelectrodes (3–5 MΩ) pulled using a Narishige PC-10 puller (Narishige Japan) or Sutter P-1000 Glass puller (Sutter Instruments) and were low-pass filtered at 3 kHz, digitized using DigiData 1440A and acquired using pClamp10 at 10-kHz sampling frequency with gains of 0.1 and 1. Recordings were performed using high chloride internal solution containing 125 mM KCl, 10 mM K-gluconate, 10 mM HEPES, 2 mM $MgCl_2$, 0.2 mM EGTA, 2 mM Na-ATP, 0.5 mM Na-GTP, and 10 mM PO creatine titrated to a pH 7.25 with KOH (pH 7.25; 270–290 mOsm) or cesium methane sulfonate ($CsMeSO_4$) internal solution containing 140 mM cesium methane sulfonate, 10 mM HEPES, 5 mM NaCl, 0.2 mM EGTA, 2 mM Mg-ATP, and 0.2 mM Na-GTP (pH 7.25; 270–290 mOsm). Biocytin (0.3%) was included in the internal solution for *post hoc* cell identification (Gupta et al., 2012; Yu et al., 2015). In experiments with KCl based internal, synaptic GABA currents were recorded in perfusing aCSF containing the glutamate receptor antagonist kynurenic acid (3 mM; Tocris). Recorded neurons were initially held at −70 mV for interneurons and −60 mV for GCs and SGCs and the response to 500-ms positive and negative current injections were examined to determine active and passive characteristics. Voltage-clamp recordings of IPSCs (spontaneous and evoked) were obtained from a holding potential of −70 mV for interneurons and −60 mV for GCs and SGCs (Yu et al., 2015; Gupta et al., 2020). $CsMeSO_4$ based internal was used to record the IPSCs as outward currents from a holding potential of at 0 mV in the absence of glutamate receptor antagonists. In some experiments tetrodotoxin (TTX; 1 μM) or gabazine (10 μM) were used to isolate action potential independent miniature IPSCs or block IPSCs, respectively. *Post hoc* biocytin immunostaining and morphologic analysis was used to definitively identify interneurons, GCs and SGCs included in this study. Morphologies were reconstructed using Neurolucida360 (Microbrightfield) for further analysis (see below, Morphometry).

Evoked IPSCs were elicited by single or paired stimulation of the PP using bipolar concentric stimulating electrodes placed at the junction of the dorsal blade and the crest, just outside the fissure (Korgaonkar et al., 2020). Constant current stimuli (0.5 μA to 5 mA) were applied using a high-voltage stimulus isolator (A365R, World Precision Instruments). The evoked mono and polysynaptic IPSCs were recorded simultaneously in GCs and SGC pairs. In some experiments, slices were exposed to

wide-field blue (λ = 470 nm) or amber (λ = 589 nm, 10 mW/mm^2) illumination using λ DG-4 Plus (Sutter Instruments) or Thorlabs 4-wavelength High-Power LED Sources (Thorlabs).

Immunohistochemistry

Following physiological recordings, slices were fixed in 0.1 mM phosphate buffer containing 4% paraformaldehyde at 4°C. For *post hoc* immunohistochemistry, slices were incubated overnight at 4°C with Alexa Fluor 594-conjugated streptavidin in 0.3% Triton X-100 and 2% normal goat serum containing PBS. Slices were mounted on glass slides using Vectashield. Sections were visualized and imaged using a Zeiss LSM 510 confocal microscope with a 0.5 numerical aperture 20× objective.

Morphometry

Stained hippocampal sections were visualized and imaged using a Nikon A1R laser scanning confocal microscope with a 20×, 0.5 NA objective lens. Cell reconstructions, from confocal image stacks, were performed using the directional kernels user-guided reconstruction algorithm in Neurolucida 360 (MBF Bioscience) followed by manual correction and validation in 3D. Approximately 10–20% of each dendritic arbor was reconstructed manually (Gupta et al., 2020). Algorithms in Neurolucida Explorer (MBF Biosciences) were used to extract nonnominal or nonordinal somatodendritic morphologic quantitative parameters for use in statistical comparisons and hierarchical cluster analysis. A total of 17 projection neurons in which the dendritic arbors were fully reconstructed were analyzed. A total of 42 somato-dendritic parameters (defined in Gupta et al., 2020) from 17 morphologically reconstructed neurons, including both features measured in Neurolucida Explorer from the 3D reconstructions and parameters measured manually in 2D rendering (Neurolucida 360, MicroBrightfield) were analyzed.

Quantification and statistical analysis

Data were tested for uniform distribution and each quantified variable was fit to the sum of two or more Gaussian functions and quality of fit determined using maximum likelihood analysis (MLA; v2test) to assess normal distribution of parameters within each cell type. Variables with a nonuniform distribution were used for subsequent cluster analysis. Hierarchical cluster analysis on principal components (HCPC) of morphologic parameters was conducted using R version 3.5.0, using R package FactoMineR by an investigator (H.X.) blinded to cell types. Hierarchical clustering on the selected principal components (PCs) was performed using Ward's criterion with Euclidean distance to generate the dendrogram. The clustering partition was obtained from hierarchical clustering and improved with K-means method (Husson et al., 2010).

Individual spontaneous, miniature and evoked IPSCs were detected using custom software in IgorPro7.0 (WaveMetrics) and different parameters were analyzed (Gupta et al., 2012). Events were visualized, and any "noise" that spuriously met trigger specifications was rejected. EPSCs were detected and analyzed using event detection in Clampfit. Kinetics and charge transfer were calculated from the averaged trace of all accepted spontaneous IPSC (sIPSC) events. Rise time was measured as the time for amplitude to change from 20% to 80% of peak. Amplitude weighted τ_{decay} was calculated from a two-exponential fit to the IPSC decay. sIPSC charge transfer was calculated as the area under the curve of the baseline adjusted average sIPSC trace. Intrinsic properties were extracted by analyzing the IV traces in Clampfit. Input resistance was calculated in response to −100-pA current injection. Spike frequency adaptation ratio was calculated as interval between the first two spikes/interval between the two last spikes in response to +70-pA current injection. Sample sizes were not predetermined and conformed with those employed in the field. Significance was set to $p < 0.05$, subject to appropriate Bonferroni correction. Statistical analysis was performed by paired and unpaired Student's *t* test (Microsoft Excel 2007) or two-way repeated measures (RM) ANOVA, one-way ANOVA, or one-way ANOVA on ranks followed by pairwise multiple comparison using Holm–Sidak method or Dunn's method (Sigma Plot 12.3) as appropriate. Data that passed normality test are shown as mean ± SEM. Data that were not distributed normally are reported as median and interquartile range (IQR) as appropriate.

Results

Quantitative morphometry resolves GCs and SGCs in mice into distinct groups

Recordings were obtained from neurons in the IML to target putative SGCs and GCL to target GCs followed by *post hoc* recovery of cell morphologies from biocytin fills (Fig. 1*A–E*). Unsupervised clustering of morphometric data obtained from reconstruction of neurons in which dendritic arbors were fully recovered was used to verify whether the somato-dendritic parameters distinguishing GCs from SGCs in mice are similar to those characterized in rats (Williams et al., 2007; Gupta et al., 2020). Projection neurons, which included GCs and SGCs, were identified based on the presence of spiny dendrites in the molecular layer and axons with mossy fiber boutons entering the hilus and targeting CA3 (Gupta et al., 2020). Morphometric parameters of the cells reconstructed in 3D were obtained using automated algorithms in Neurolucida Explorer (defined in Gupta et al., 2020). PC analysis (PCA) of 42 morphometric parameters from 17 cells revealed that the first two PCs explained >50% of the total variance in the data, while the first seven components explained 90% of the variance. HCPC on the first seven PCs suggested partitioning of cells into three clusters (Fig. 1*F*) as illustrated on the factor map produced by the first seven PCs (Fig. 1*G*). Despite the exclusion of categorical variables such as soma location from HCPC, cells classified as GCs and SGCs by investigator (M.A.) segregated into two distinct clusters based on Dimension1 (Dim1). Interestingly, cells classified as GCs further segregated into two clusters (Clusters #1 and #2) based on Dim2. Variables >70% correlated with the first PC were identified as most responsible for PC formation. Evaluation of the quantitative variables underlying the clusters revealed that cluster #3, comprised of putative SGCs, was distinguished by a higher number of primary dendrites, greater dendritic angle, soma width, and cell surface area and lower dendritic complexity (Fig. 1*H–J*). While cells in Cluster #1 had fewer, typically one, primary dendrite, lower dendritic angle, and higher dendritic complexity (Fig. 1*H–J*), Cluster #2 segregated based on the presence of more fourth order segments, ends and intersections. Interestingly, dendritic angle was different between groups, increasing from Cluster #1 to Cluster #3 (Fig. 1*H*). The number of primary dendrites in Cluster #3 (putative SGCs) was significantly higher than in both Clusters #1 and #2 (Fig. 1*I*). Similarly, Cluster #3 (putative SGCs) had the least dendritic complexity which was significantly lower than in Cluster #1 while differences in dendritic complexity between Clusters #1 and #2 failed to reach statistical significance (Fig. 1*J*).

Morphometric parameters from putative GCs (Clusters #1 and #2) were pooled together and compared with Cluster #3 (putative SGCs) for further analysis. Like GCs, SGC axons extended to CA3 and showed mossy fiber terminals in the hilus (Fig. 2*A*, *B*), consistent with features of a projection neuron. Similar to findings in rats (Gupta et al., 2020), GCs and SGCs differed in dendritic angle, number of primary dendrites, soma aspect ratio and dendritic complexity (Fig. 2*C–F*; Table 1). In contrast, certain global parameters such as total number of dendritic ends and total length of dendrites were not different between the cell

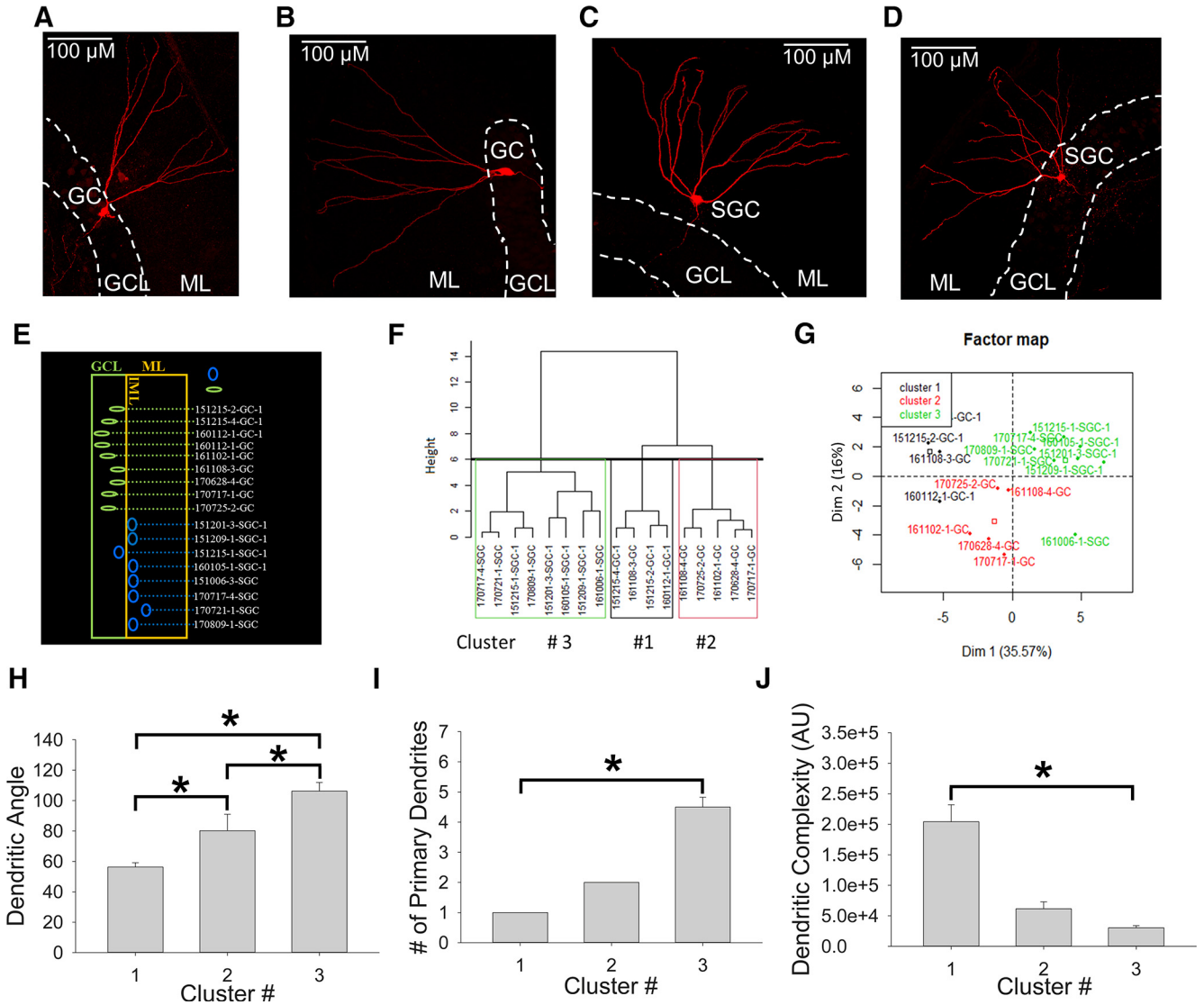

Figure 1. GCs and SGCs cluster into distinct subtypes on the basis of morphology. ***A–D***, Example images of GCs (***A***, ***B***) and SGCs (***C***, ***D***) illustrate the somatic location and dendritic spread. Note that reconstruction of neuron in ***A*** is presented in Figure 2*A*. Scale bar: 100 µm. ***E***, Schematic of the somatic location of the cells included in the cluster analysis. The GCL is illustrated as a green box and IML as an orange box with somata illustrated in blue and GCs in green. All images were obtained a 20× magnification. GCL, granule cell layer; ML, molecular layer. ***F***, Dendrogram generated by HCPC based on 42 morphometric parameters (defined in Gupta et al., 2020) using Ward's method with Euclidean distance suggests three putative clusters. ***G***, Factor map base on first seven PCs. ***H–J***, Summary data of dendritic angle (***H***), number of primary dendrites (***I***), and dendritic complexity (***J***) for cells in the three clusters. Data are presented as mean ± SEM; $*p < 0.05$ by one-way ANOVA followed by pairwise comparison with Holm–Sidak method for ***H*** and $p < 0.05$ by one-way ANOVA on ranks followed by pairwise comparison with Dunn's method for ***I***, ***J*** where the data failed Shapiro–Wilk normality test. A.U., arbitrary units.

types (Fig. 2*G*,*H*; Table 1). Together, these data provide a comprehensive morphometric comparison of GCs and SGCs in mice. Our results confirm that the presence of three or more primary dendrites and wide dendritic angle reliably distinguishes SGCs from GCs as reported in recent studies (Save et al., 2018; Gupta et al., 2020; Rovira-Esteban et al., 2020).

SGCs differ from GCs in intrinsic physiology and frequency of basal synaptic inhibition

Examination of active and passive responses to graded current injections revealed no difference in firing frequency between the two cell types (Fig. 2*I–K*). However, input resistance was significantly lower in SGCs (Fig. 2*K*). Spike frequency adaptation ratio (ratio of inter-spike interval between first two and last two spikes during a +70-pA current injection) in SGCs was lower than in GCs (Fig. 2*L*). These findings are consistent with differences in intrinsic properties identified between the SGCs and GCs (Williams et al., 2007; Gupta et al., 2012; Save et al., 2018).

sIPSCs, recorded from holding potential of −60 mV in the presence of glutamate blockers, were more frequent in SGCs (sIPSC frequency in Hz, GCs: 8.38 ± 1.14, $N = 18/12$ mice, SGCs: 13.48 ± 1.07, $N = 19/13$ mice, $p = 0.003$, *t* test; Fig. 3*A*,*C*). However, sIPSCs amplitude (sIPSC amplitude in pA, GCs: 42.98 ± 3.35, $N = 18$, SGCs: 41.52 ± 3.01, $N = 19$, $p = 0.75$, *t* test; Fig. 3*D*), amplitude weighted decay time constant ($\tau_{decay\text{-}WT}$ in ms, GCs: 3.31 ± 0.22, $N = 18$, SGCs: 3.2 ± 0.2, $N = 19$, $p = 0.72$, *t* test) and 20–80% rise times (in ms, GCs: 0.22 ± 0.01, $N = 18$, SGCs: 0.20 ± 0.0, $N = 19$, $p = 0.13$, *t* test) were not different between GCs and SGCs (Fig. 3*B*,*D–F*). These findings demonstrate that SGCs in mice show the same structural and functional distinctions from GCs identified in prior studies in rats (Gupta et al., 2012, 2020). These data validate the morphologic criteria which we used to distinguish GCs and

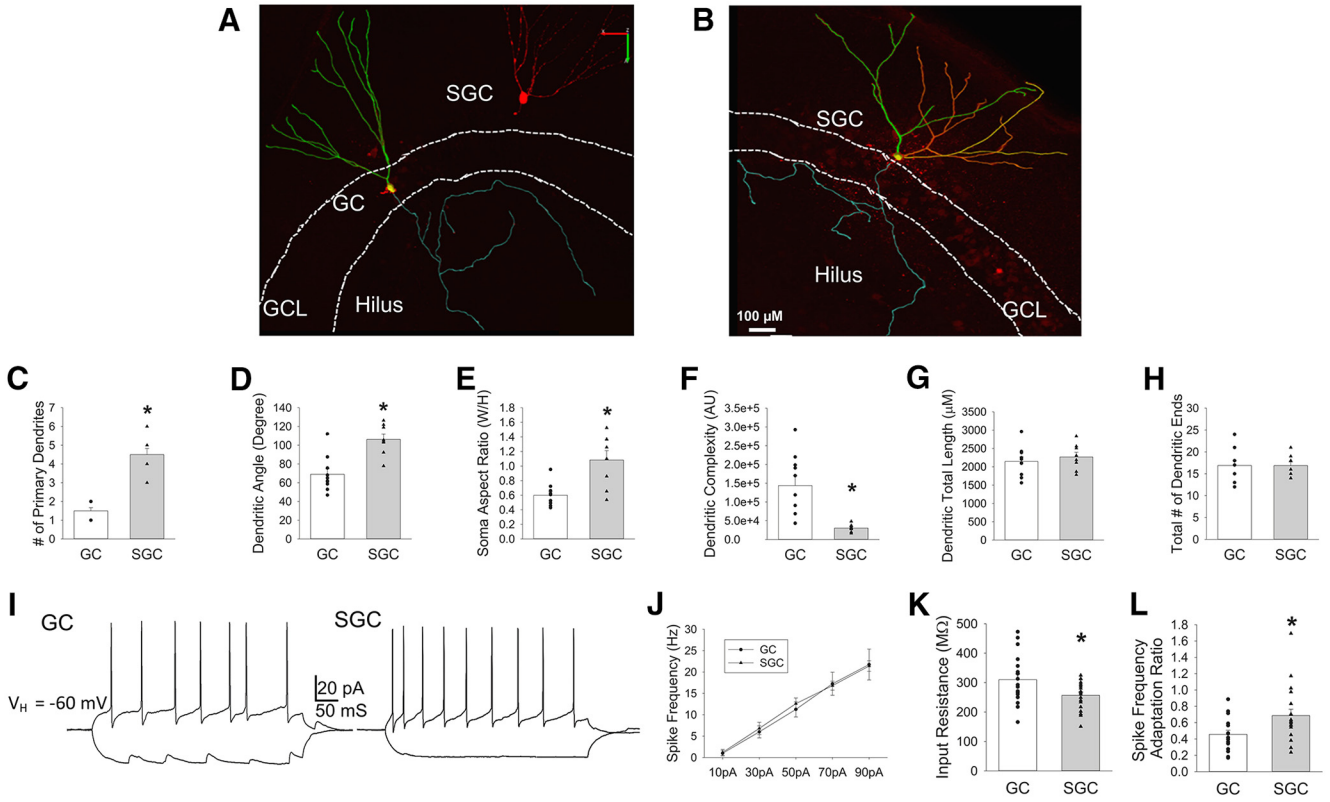

Figure 2. Morphologic and physiological characteristics of GCs and SGCs in mice. ***A***, ***B***, Overlay of confocal image and Neurolucida 360 reconstruction of a biocytin filled GC (***A***) and SGC (***B***) show dendritic arbors and axon projection toward CA3. Cyan: axons; orange, green, yellow: dendritic trees. ***C–H***, Summary plots of morphologic parameters including number of primary dendrites (***C***), dendritic angle (***D***), soma aspect ratio (***E***), dendritic complexity (***F***), dendritic total length (***G***), and total number of dendritic ends (***H***) between GCs ($n = 10$) and SGCs ($n = 8$). ***I***, Voltage traces in response to +70- and −100-pA current injections in a GC (left) and SGC (right) illustrate firing pattern and passive properties. ***J***, Summary plot of firing frequency in response to increasing current injections in GCs ($n = 8$) and SGCs ($n = 10$). ***K***, ***L***, Summary histogram of input resistance (measured from response to −100 pA; ***K***) and spike frequency adaptation ratio (***L***) in GCs ($n = 18$) and SGCs ($n = 19$). Data presented as mean ± SEM; $*p < 0.05$ by independent *t* test.

Table 1. Summary of morphometric and physiology data in GC and SGCs

Figure	Parameter (unit)	Cluster 1 (5 cells/8 mice)	Cluster 2 (4 cells /8 mice)	Cluster 3 (8 cells/8 mice)	*F* and *P* value
1*H*	Dendritic angle (degree)	56.28 ± 2.84	80.21 ± 10.82	105.12 ± 6.17	$F_{(2,14)} = 16.13$, $p < 0.001$ by one-way ANOVA Clu1 vs Clu2 = 0.038 Clu1 vs Clu3 < 0.001 Clu2 vs Clu3 = 0.032
1*I*	Number of primary dendrites (count)	1.00 ± 0.00	2.00 ± 0.00	4.60 ± 0.40	<0.001 by Kruskal–Wallis ANOVA on ranks Clu1 vs Clu2 = 0.038 Clu1 vs Clu3 < 0.001 Clu2 vs Clu3 = 0.032
1*J*	Dendritic complexity (A.U.)	204,147 ± 27,920	61,393 ± 11,452	30,435 ± 4609	0.002 by Kruskal–Wallis ANOVA on ranks Clu1 vs Clu2 > 0.05 Clu1 vs Clu3 < 0.05 Clu2 vs Clu3 > 0.05
Figure	Parameter (unit)	GC	SGC		*P* value by independent Student's *t* test
2*C*	Number of primary dendrites (count)	1.50 ± 0.17	4.5 ± 0.33		1.90E-07
2*D*	Dendritic angle (degree)	69.00 ± 5.98	106.23 ± 5.71		0.0004
2*E*	Soma aspect ratio	0.60 ± 0.05	1.08 ± 0.13		0.001
2*F*	Dendritic complexity (A.U.)	143,653.30 ± 26,506.76	30,290.86 ± 3515.42		0.002
2*G*	Total dendritic length (μm)	2147.37 ± 128.20	2269.97 ± 126.30		0.512
2*H*	Total dendritic ends (count)	16.90 ± 1.13	16.87 ± 0.81		0.986
2*K*	Input resistance (MΩ)	309.89 ± 19.58	229.33 ± 29		0.031
2*L*	Spike frequency adaptation ratio	0.45 ± 0.05	0.68 ± 0.07		0.023

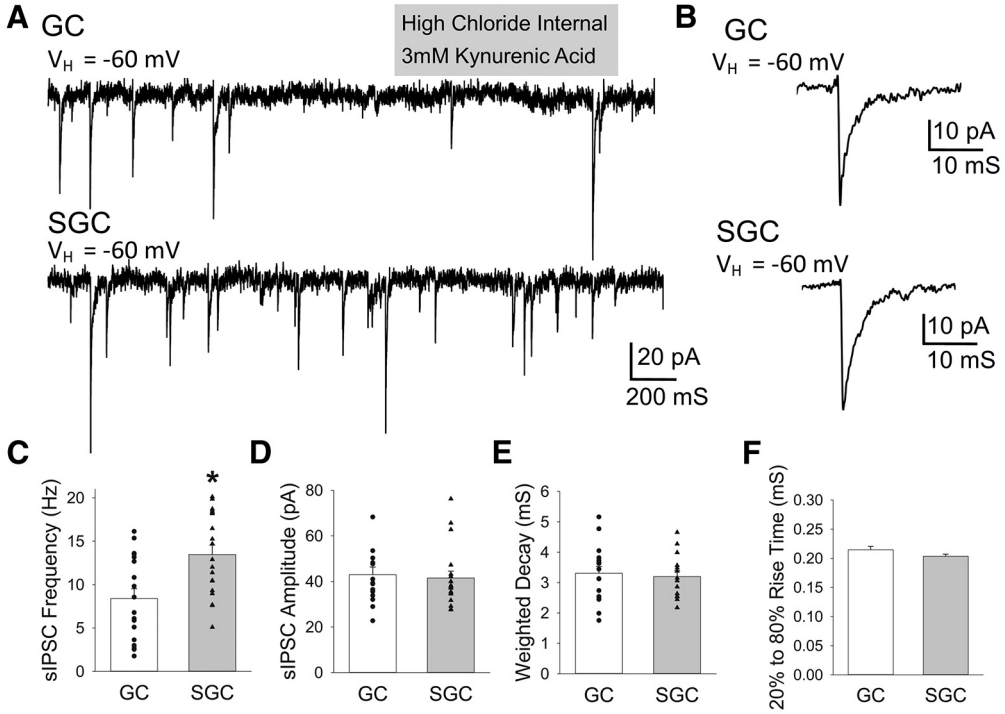

Figure 3. SGCs receive more spontaneous inhibitory synaptic events than GCs. ***A***, Representative current traces from a holding potential of −60 mV illustrate sIPSCs in a GC (above) and SGC (below). Text in gray box indicates recording condition. ***B***, Example of average sIPSC trace from a GC (above) and SGC (below). ***C–F***, Summary histogram of sIPSC frequency (***C***), amplitude (***D***), amplitude weighted decay time constant (***E***), and 20–80% rise time (***F***) in GCs ($n = 18$) and SGCs ($n = 19$). Data presented as mean ± SEM; $*p < 0.05$ by independent t test.

SGCs in the subsequent experiments and indicate differences in inhibitory inputs between the cell types.

Limited role of PV-INs in steady-state synaptic inhibition of GCs and SGCs in slices

To determine whether differential inputs from PV-INs, contribute to the higher action potential-dependent sIPSCs frequency in SGCs we examined whether optical suppression of PV-INs in mice expressing the inhibitory opsin, halorhodropsin (NpHR3), under control of the PV promotor reduced sIPSC frequency. Unlike archaerhodopsin and chloride conducting channelrhodopsins which can depolarize terminals and induce synaptic release, NpHR3 has been shown to hyperpolarize neurons without triggering transmitter release making it the ideal choice to examine synaptic release (Mahn et al., 2016). Validity of the PV-Cre mouse line was confirmed by colocalization of PV and YFP using immunostaining (data not shown) and by fast, nonadapting firing in recordings from YFP positive neurons (Fig. 4*A*). Since activation of NpHR3 can reduce the chloride gradient (Alfonsa et al., 2015), light exposure was restricted to 2-s periods. Recordings from YFP labeled neurons established that the 2-s amber light illumination reliably and reversibly hyperpolarized YFP positive fast spiking neurons (n > 10 cells) and suppressed action potential firing (Fig. 4*A*). sIPSCs were recorded from GCs and SGCs for a total of 7 min: recordings started with a 2-min baseline followed by five 1-min cycles with a 2-s exposure to amber light at the beginning of each cycle followed by time for recovery of the chloride gradient between light exposure (Fig. 4*B*). sIPSC parameters measured during the 2 s before light exposure were averaged and compared with the parameters averaged over the periods during the five cycles of light exposure. Contrary to expectations, optical suppression of PV-INs failed to reduce both frequency (in Hz, GC no-light: 14.19 ± 2.5; GC amber light: 13.6 ± 2.4, $N = 5/3$ mice, $p = 0.61$, paired t test) and amplitude (in pA, GC no-light: 46.65 ± 9.62; GC amber light: 45.13 ± 5.94, $N = 5/3$ mice, $p = 0.42$, paired t test) of GC sIPSCs (Fig. 4*C–E*). Similarly, optical suppression of PV-IN firing failed to reduce sIPSC frequency (in Hz, SGC no-light: 15.62 ± 2.6; SGC amber light: 14.69.6 ± 2.0, $N = 5/3$ mice, $p = 0.79$, paired t test) and amplitude (in Hz, GC no-light: 43.18 ± 5.1; GC amber light: 40.95 ± 3.2, $N = 5/4$ mice, $p = 0.42$, paired t test) in SGCs as well (Fig. 4*C–E*). These data raise a surprising possibility that PV-INs may not contribute to basal sIPSCs in either GCs or SGCs in acute slice preparations.

Given the unexpected outcome, and since the optogenetic system was functionally validated (Fig. 4*A*), we considered whether use of glutamate receptor antagonist to isolate IPSCs may have reduced PV-IN firing and underestimated their contribution to sIPSCs. To address this possibility, IPSCs were recorded as outward currents from cells held at 0 mV (reversal for glutamatergic currents) using a low chloride internal. As expected, sIPSC frequency recorded in the absence of glutamate blockers was higher (Fig. 4*F–H*) than that recorded in glutamate receptor blockers (Figs. 3, 4*C,D*) in both cell types. Nevertheless, sIPSC frequency and amplitude in GCs were not reduced by amber light suppression of PV-INs (frequency in Hz, no-light: 26.80 ± 3.78, light: 28.32 ± 2.41, $N = 13/8$ mice, $p = 0.49$, paired t test; amplitude in pA, no-light: 26.43 ± 2.88, light: 25.46 ± 2.10, $N = 13/8$ mice, $p = 0.76$, paired t test; Fig. 4*F–H*). Similarly, sIPSC parameters in SGCs were also unaltered during amber light exposure (frequency in Hz, no-light: 35.77 ± 5.44, light: 36.81 ± 4.48, $N = 11/8$ mice, $p = 0.66$, paired t test; amplitude in pA, no-light: 28.96 ± 3.72, light: 26.74 ± 3.17, $N = 11/8$ mice, $p = 0.25$, paired t test; Fig. 4*F–H*). Together, these data obtained under two different recording conditions support the surprising conclusion that PV-INs contribute minimally to basal sIPSC frequency in both dentate projection neuron subtypes.

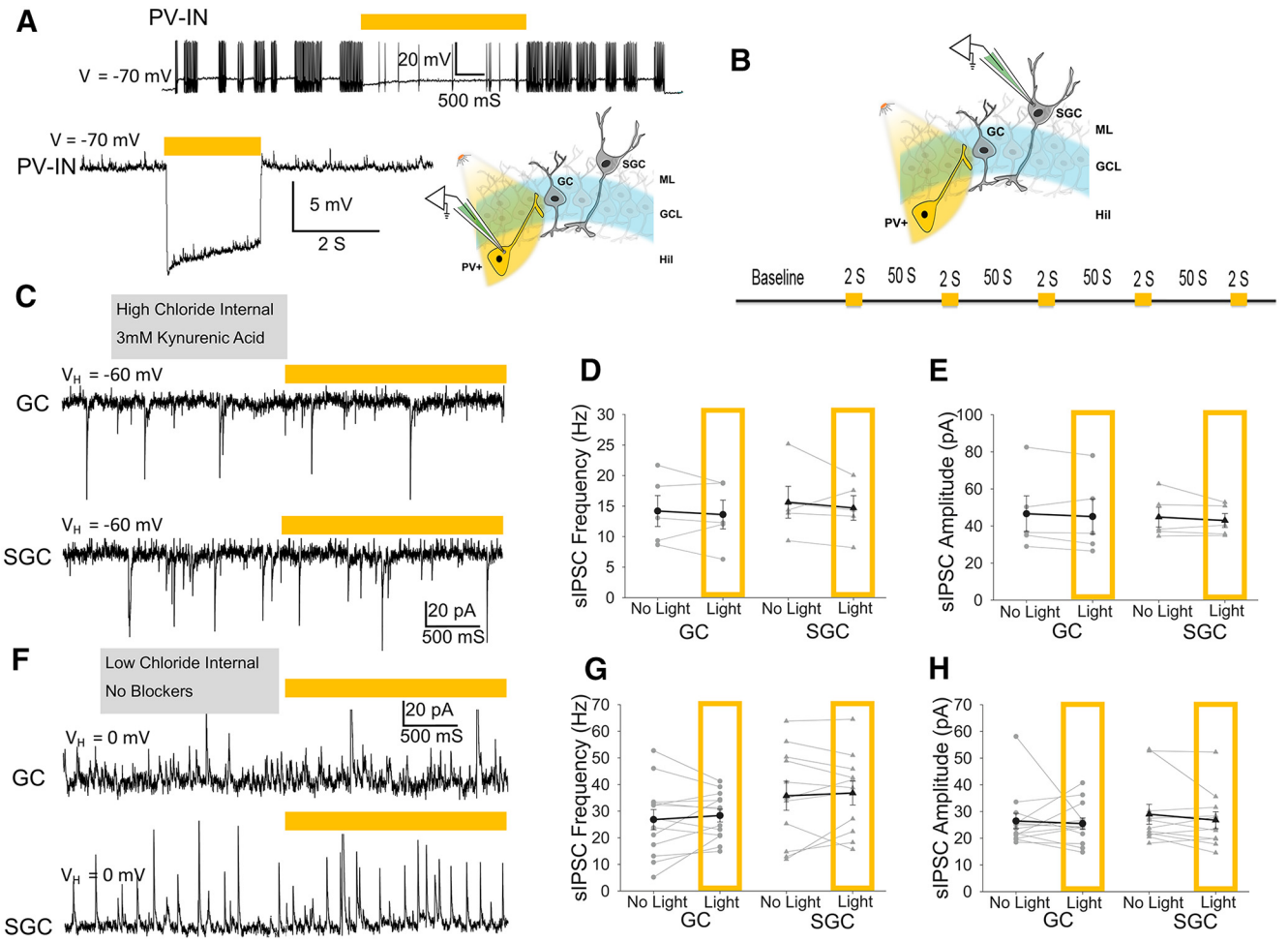

Figure 4. Optical suppression of PV-INs fails to reduce sIPSC frequency in both GCs and SGCs. ***A***, Representative membrane voltage trace (above) from a holding potential of −70 mV in a YFP-positive PV interneuron expressing halorhodopsin in the GC-hilar border illustrates the high-frequency firing during depolarizing current injection (100 pA for 10 s) and the ability of amber light (bar above) to suppress firing. Representative trace from 19 trials in four cells. Membrane voltage trace from an NpHR3-YFP expressing PV-IN shows rapid and reversible hyperpolarization (below) during the 2-s amber light stimulation. Schematic to the right illustrates recording condition and optical stimulation. ***B***, Schematic of the experimental paradigm illustrates amber light stimulation of NpHR3-YFP expressing PV-IN while recording from GC/SGC (above) and the protocol for light OFF and light ON condition below. ***C***, Current traces from a GC (above) and SGC (below) recorded from a holding potential of −60 mV using high-chloride internal shows sIPSCs as inward currents before and during NpHR3 activation (amber bar) in PV-INs. IPSCs were isolated in kynurenic acid (3 mM). ***D***, ***E***, Plots summarize effect of optical suppression of PV-IN on sIPSC frequency (***D***) and amplitude (***E***; $n = 5$ GCs and SGC). ***F***, Representative traces illustrate sIPSCs in a GC (above) and SGC (below) before and during activation amber light exposure (amber bar). Recordings were obtained using a low-chloride internal from a holding potential of 0 mV without synaptic blockers. ***G***, ***H***, Summary plots of effect amber light on sIPSC frequency (***G***) and amplitude (***H***) in GCs ($n = 13$) and SGCs ($n = 11$). Data presented as mean ± SEM. Text in gray box indicates recording condition.

While unlikely, a potential reason for the above outcome is that a majority of the sIPSCs in our recordings were action potential independent miniature events, which would not be modified by suppressing PV-IN firing. To exclude this possibility, we tested the ability of the sodium channel antagonist TTX (1 μM) to reduce frequency of IPSCs indicating the presence of action potential driven events. As expected based on prior studies (Otis et al., 1991; Goswami et al., 2012), TTX significantly reduced IPSC frequency in both GCs (frequency in Hz, before ACSF: 11.58 ± 1.58, TTX: 1.4 ± 0.44 $N = 7$, $p = 0.0003$, paired t test) and SGCs (frequency in Hz, before ACSF: 10.83 ± 2.09, TTX: 1.96 ± 0.9 $N = 5$, $p = 0.001$, paired t test). TTX also reduced IPSC amplitude in both cell types (data not shown). Overall, the ability of TTX to suppress IPSC frequency indicates that majority of sIPSCs in both SGCs and GCs are driven by interneuron firing. Taken together, these data support the conclusion that PV-INs do not contribute significantly to action potential driven basal sIPSCs in both GCs and SGCs in slice preparations.

Activation of PV-INs drives synaptic inhibition in both GCs and SGC

Since sIPSCs represent synaptic inhibition in the absence of afferent inputs, we examined whether direct optical activation of PV-IN evoked IPSCs (oeIPSCs) in GCs and SGCs in slices from mice expressing channelrhodopsin (ChR2) in PV-INs. Following baseline recordings of sIPSCs in glutamate antagonist without light, recordings were continued during optical activation of ChR2 in PV-IN using blue light (λ = 473 nm, 10 s). Optical activation of PV-INs elicited a significant increase in IPSC frequency in GCs (frequency in Hz, no-light: 8.45 ± 1.31, light: 52.11 ± 5.92, $N = 14/8$ mice, $p = 2E\text{-}06$, paired t test; Fig. 5*A–C*) confirming the robust PV-IN input to GCs. PV-IN activation increased IPSC frequency in SGCs as well (frequency in Hz, no-light: 13.68 ± 1.20, light: 59.49 ± 4.62, $N = 14/9$ mice, $p = 2E\text{-}07$, paired t test; Fig. 5*A–C*), demonstrating functional PV-IN innervation of SGCs. However, IPSC peak amplitude was not increased by optical activation of PV-INs in either GCs or SGCs (Fig. 5*D–F*). These data demonstrate that SGCs, like GCs, receive PV-IN

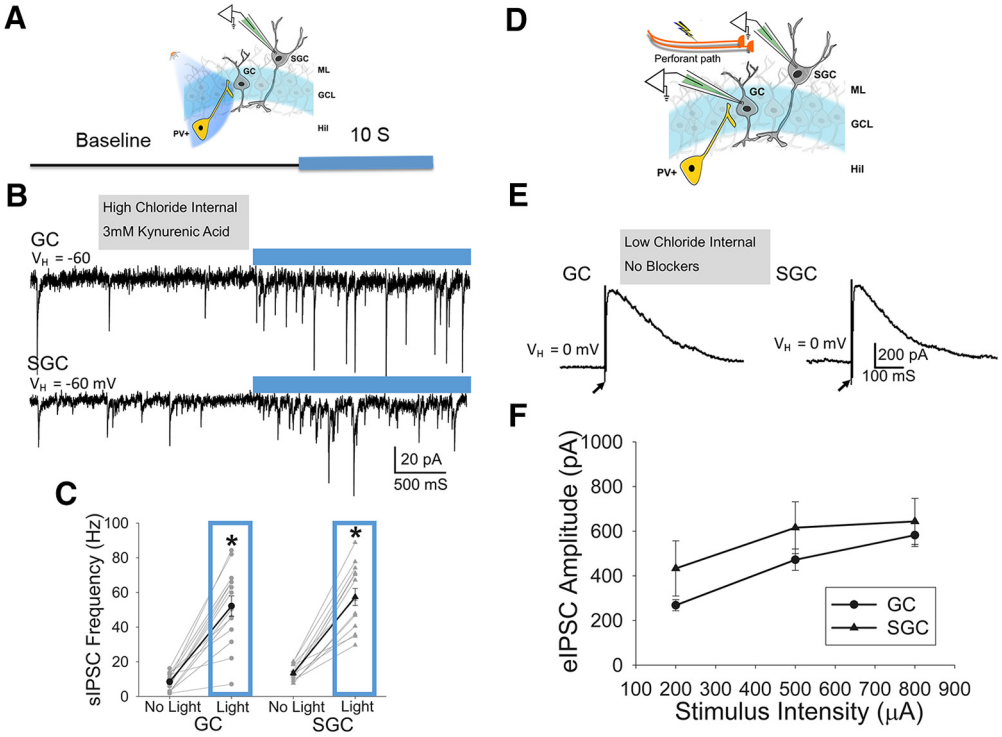

Figure 5. Activation of PV-INs and afferent stimulation evoke inhibitory synaptic currents in both dentate projection neuron subtypes. ***A***, Schematic illustrates blue light stimulation of ChR2-YFP expressing PV-IN while recording from GC/SGC (above) and light OFF and light ON protocol below. ***B***, Example recordings from a GC (above) and SGC (below) illustrate sIPSCs before and during optical activation of PV-INs. Cells were held at −60 mV and kynurenic acid (3 mM) was used to isolate IPSCs. ***C***, Summary plots of sIPSC frequency before and during blue light exposure in GCs ($n = 14$) and SGCs ($n = 14$). ***D***, Schematic of the experimental paradigm illustrates PP stimulation while recording from GC/SGC. ***E***, PP-evoked IPSC in GC and SGC recorded as outward currents using a low-chloride internal and a holding potential of 0 mV. ***F***, Summary plot of eIPSC peak amplitude in GCs and SGCs in response to stimulation of the PP at increasing current intensities. Data presented as mean ± SEM; $*p < 0.05$ by paired *t* test (in panel ***C***) or unpaired *t* test (in panel ***D***). Text in gray box indicates recording condition.

inputs and that direct activation of PV-INs leads to an increase in synaptic inhibitory events in both GCs and SGCs. Since PV-INs are known to be recruited during PP activation and support feedforward and feedback GC inhibition (Ewell and Jones, 2010), we examined whether recruitment of inhibition by afferent stimulation differed between the cell types. Single PP stimulation at increasing intensities evoked IPSCs in both SGCs and GCs. The peak amplitude of afferent evoked IPSCs was not different between cell types ($N = 12$ cells each from 8 mice, $F_{(1,10)} = 0.874$, $p = 0.37$ by two-way RM ANOVA; Fig. 5*E*,*F*), demonstrating that both GCs and SGCs receive similar early feedforward/feedback inhibition on single PP stimulation.

Afferent stimulation drives greater enhancement of sustained feedback inhibition in GCs

A functional characteristic of SGCs, not observed in GCs, is their unique ability for sustained firing in response to paired afferent stimuli in rat hippocampal slices, which has been proposed to drive feedback inhibition and sculpt pattern separation (Larimer and Strowbridge, 2010). We examined the reliability and reproducibility of SGC sustained firing in SGCs in mice. As is typical for GCs, a single PP stimulus evoked a single action potential in GCs (3/3 cells tested) as well as in SGCs (4/4 cells tested) but failed to elicit sustained spiking (data not shown). However, when the PP was stimulated with a pair of suprathreshold stimuli at 10-ms interval, consistent with theta frequency inputs (Larimer and Strowbridge, 2010; Braganza et al., 2020), a subset of SGCs showed prolonged spiking activity. Sustained firing was observed in 51.51% of the trials (17/33 of trials in 2/4 SGCs; Fig. 6*A*,*B*). The sustained firing was initiated between 200 ms to 2 s after the paired stimulation, although the latency to sustained firing was over 6s in a few trials indicating that the sustained firing was mediated by network effects (median 1.14 s, IQR: 0.61–1.9 s; Fig. 6*C*). This evoked sustained firing in SGC lasted several seconds, at times until the end of the recording 20 s after stimulation (Fig. 6*D*). On average, the sustained firing lasted 15 s, which is likely an underestimate because of the termination of recordings. None of the GCs tested exhibited firing beyond the early evoked firing in any of the trials (0/12 trials, three GCs).

Sustained firing in SGCs has been correlated with hilar mossy cell and interneuron firing as well as reduced GC excitability (Larimer and Strowbridge, 2010). However, whether GCs receive enhanced synaptic inhibition during this period and whether SGCs undergo a parallel sustained increase in feedback synaptic inhibition is not known. Using simultaneous recordings in GC-SGC pairs (Fig. 6*E*), we directly compared recruitment of polysynaptic sustained inhibition in GCs and SGCs following paired PP stimulation. Representative image of cells filled during paired recordings show the GC with soma located in the cell layer and SGC somata in the IML (Fig. 6*G*). Paired PP stimuli elicited a large early eIPSC peak (Fig. 6*E1*, insets) followed by a prolonged barrage of "evoked-sustained" IPSCs (esIPSCs) lasting over 20 s in both GCs and SGCs (Fig. 6*E1*). To better characterize the evoked sustained activity, we binned IPSCs into 5-s segments before the stimulus and 1-s segments 500 ms to 10.5 s after the stimulation, with additional 5-s segments 15–20 and 25–30 s poststimulus (Fig. 6*F*). The 500 ms immediately following stimulation was not included in the analysis to avoid the period of maximum evoked IPSC conductance which included summated events and obscured individual events. The peak IPSC frequency

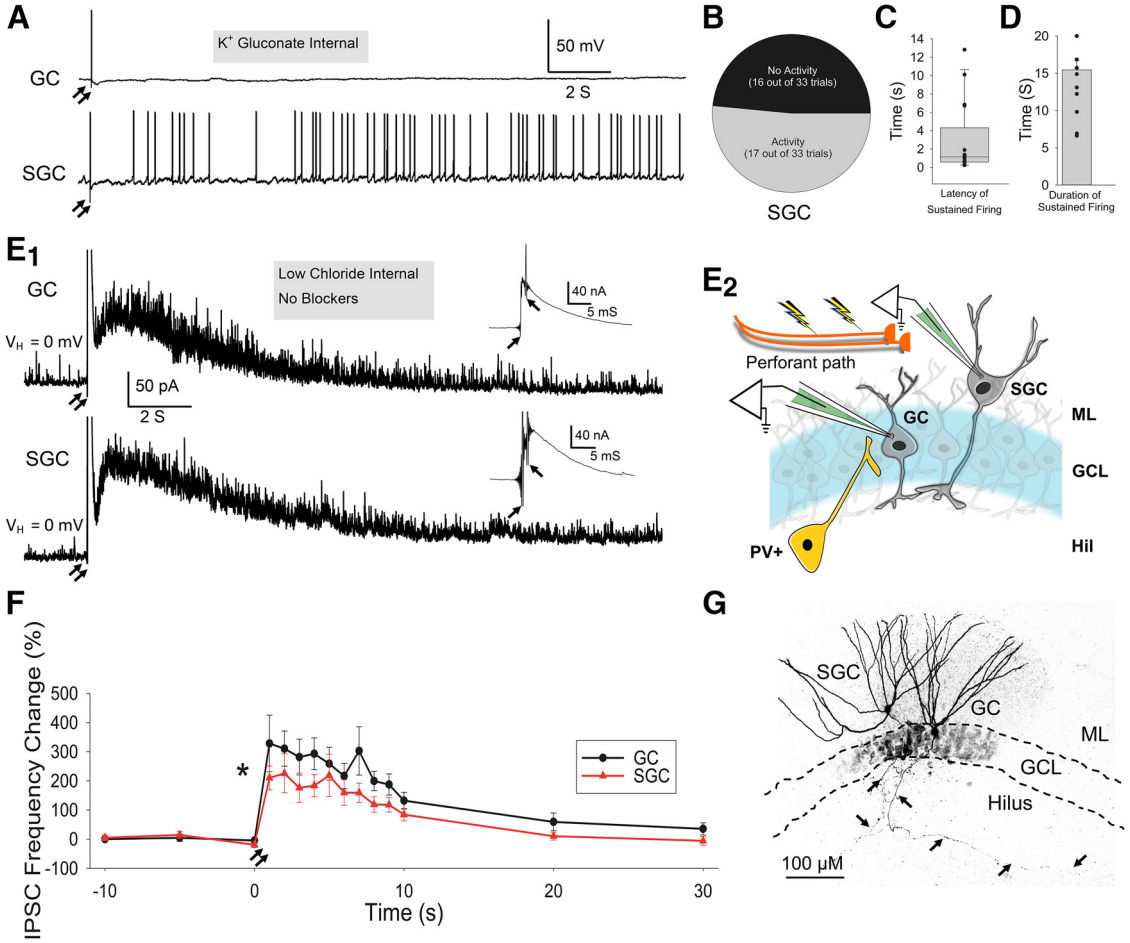

Figure 6. Afferent evoked prolonged SGC firing is associated with sustained increase in sIPSC frequency in both GC and SGC. ***A***, Membrane voltage traces in a GC (above) and SGC (below) evoked by a pair of suprathreshold stimuli to the PP (denoted by two arrows). Note prolonged firing in the SGC while none of the GCs ($n = 3$ cells, 12 trails) showed more than one to three spikes. ***B***, Plot shows the proportion of trials that evoked sustained firing in SGCs ($n = 4$ cells, 33 trials). ***C***, ***D***, Plots illustrate the distribution of latency from afferent stimulation to the start of sustained firing (***C***) and duration of sustained firing in SGCs recorded for a maximum of 20 s after stimulation. ***E***, Schematic of paired GC-SGC recordings in response to paired PP stimulation (***E$_2$***). Current traces of simultaneously recorded GC-SGC pair illustrate the sustained increase in IPSC frequency compared with prestimulus baseline (***E$_1$***). The eIPSC peak is truncated to better illustrate the sustained change in IPSCs over 20 s. ***E$_1$***, insets, Traces at a different scale illustrate the peak eIPSC amplitude. ***F***, Summary plot of sIPSC frequency in GCs and SGCs ($n = 12$ each) before stimulation (binned over 5 s) and evoked sustained IPSC frequency (1-s bins for the first 10- and 5-s bins at 20 and 30 s) for success rate in induction of prolonged spiking activity in GCs (12 trials, $N = 3$) and SGCs (33 trials, $N = 5$). ***G***, Maximum intensity projection of a confocal image stack of a GC-SGC pair filled during recordings (presented as gray scale and inverted) illustrate dendric arbors and hilar axon (arrows). GCL, granule cell layer; ML, molecular layer; GC, granule cell; SGC, semilunar granule cell. Data presented as median (IQR) for in ***C*** and mean ± SEM in ***D***, ***F***; $*p < 0.05$ for effect of cell-type ($F_{(1,11)} = 4.9$) by two-way RM ANOVA. Text in gray box indicates recording condition.

following paired PP stimulation (500–1500 ms) showed high variability and was not different between cell types (in Hz, GC: 64.7 ± 4.3; SGC: 72.9 ± 5.3, $n = 12$ each $p > 0.05$ by unpaired Student's t test). Although the sIPSC frequency before stimulation was stable within each cell, there was considerable cell-to-cell variability. To normalize for the variability and assess relative change in esIPSC frequency, the difference in IPSC frequency following stimulation was normalized to the prestimulus sIPSC frequency averaged over 3×5 s prestimulus bins [(post-pre)/pre*100]. Both GCs and SGCs showed a significant poststimulus increase in esIPSC frequency lasting over 20 s. In addition to the significant effect of time, the difference between cell types was statistically significant ($F_{(1,11)} = 9.4$, for effect of time and $F_{(1,11)} = 4.9$ for cell-type, $p < 0.05$ by two-way RM ANOVA; Fig. 6*F*). Pairwise comparison between cell types, revealed that the increase in esIPSC frequency normalized to prestimulus frequency was significantly greater in GCs than in SGCs. Both GCs and SGCs showed increase in esIPSC frequency for up to 10 s poststimulus reaching similar maximum frequency and declining back to prestimulus levels by 20–30 s. However, the relative increase in esIPSC frequency (normalized to prestimulus frequency) quantified over the first 500–1500 ms (1 s) after stimulation was significantly higher in GCs than in SGCs ($p < 0.05$, by two-way RM ANOVA followed by pairwise multiple comparison using Holm–Sidak method).

Interestingly, not all cells showed robust esIPSC barrages even within the same slice, suggesting cell specific recruitment of feedback inhibition. We found that 16.67% (2/12) GCs and 33.33% (4/12) SGCs failed to show esIPSC barrage, defined as doubling in basal frequency in the first three poststimulus bins examined (3 s). Additional recordings conducted in the presence of the $GABA_A$ receptor antagonist, gabazine (10 μM) confirmed that, like eIPSC, esIPSCs were also eliminated by gabazine (data not shown). These results demonstrate that paired PP stimulation results in prolonged changes to dentate inhibition and SGC excitability. Crucially, the data reveal that the relative increase in sustained feedback inhibition in SGCs is less than in GCs and suggest that despite their higher basal synaptic inhibitory tone, SGC show lower increase in inhibitory gating than GCs following activation of inputs.

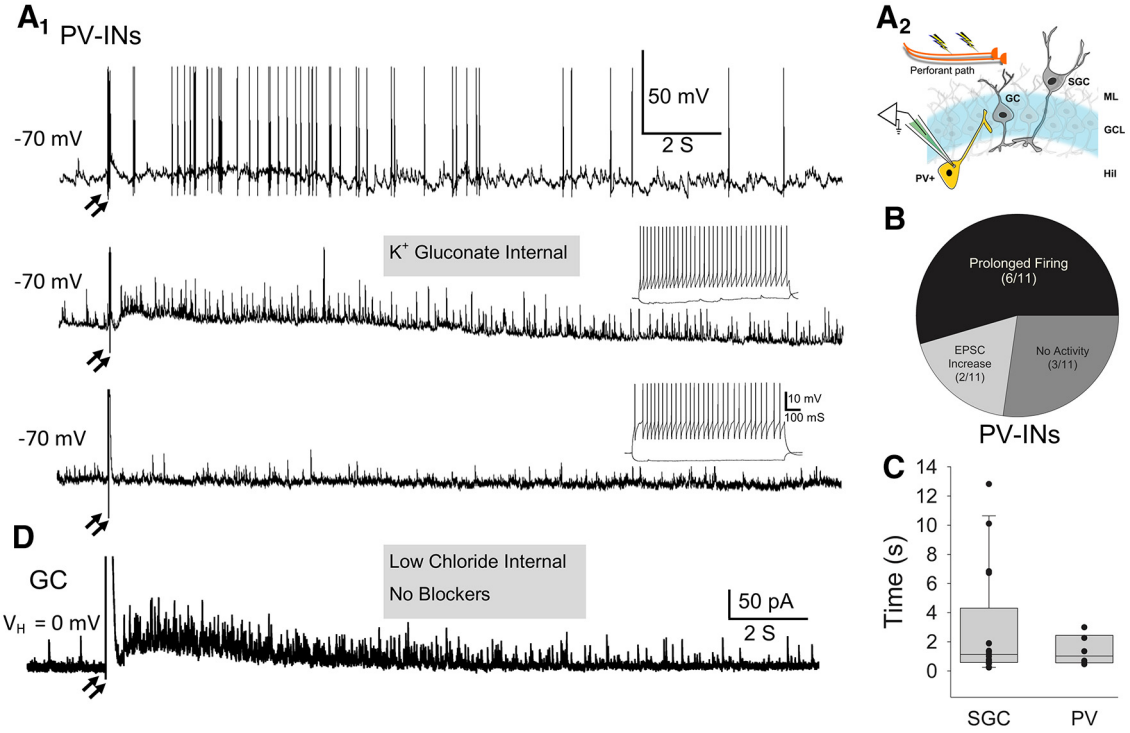

Figure 7. Increase in PV-IN excitability during evoked sustained sIPSCs in dentate projection neurons. ***A***, Example traces show increased firing (above), enhanced EPSP barrages (middle) and unaltered EPSP frequency (below) in YFP-positive PV-INs (***A1***) in response to the paired PP stimulation paradigm (denoted by two arrows) illustrated in ***A2***. Insets in middle and lower traces illustrate high-frequency firing in recorded PV-IN. ***B***, Pie chart summarizes the proportion of PV-INs that showed evoked sustained firing, EPSP increase or no change in response to stimulation ($n = 11$ cells, 33 trials). ***C***, Plot illustrates the distribution of latency of enhanced PV-IN firing following paired PP stimulation. ***D***, Current traces from a GC showing sustained IPSCs is included for comparison. Text in gray box indicates recording condition.

Role of PV-INs in sustained feedback inhibition of dentate projection neurons following paired afferent stimulation

Since PV-INs are known to mediate strong GC feedforward and feedback inhibition (Hefft et al., 2002), we examined whether they exhibit sustained firing in response to paired PP stimuli coinciding with increased esIPSCs in GCs. PV-INs in the hilar GC border were identified based on YFP labeling and confirmed by the high-frequency, nonadapting firing (Fig. 7*A1*, insets). PV-IN voltage traces in responses to paired PP stimulation (Fig. 7*A*) are illustrated alongside the time course of esIPSC in a GC (Fig. 7*D*) for reference. A subset of PV-INs (4/11 cells, 36.4%) exhibited spontaneous action potential firing at rest under our recording conditions. Interestingly, only 54.5% (6/11 cells) PV-INs showed sustained increase in firing on paired PP stimulation. An additional 18.2% (2/11 cells) PV-INs received increased EPSC drive during this period suggesting that they may be driven by SGC firing (Fig. 7*B*). However, 27.3% (3/11) PV-INs showed no apparent sustained change in EPSC frequency on PP stimulation despite the early evoked firing. When present, the prolonged PV-IN firing followed the initial stimulation with a median latency of 1.02 s (IQR 0.62–2.03 s) which was similar to the latency to evoked SGC firing (Fig. 7*C*). Since SGCs and not GCs show evoked sustained firing following paired PP stimulation, these data suggest that the sustained firing in SGCs likely drives PV-IN firing. These results raise the possibility that PV-IN firing contributes to a certain component of esIPSCs in GCs and SGCs.

To verify whether halorhodopsin suppression could reduce PP-evoked PV-IN firing, we performed control recordings from YFP-labeled neurons in PV-NpHR3 mice. While optical suppression failed to fully eliminate firing of PV-INs in response to paired PP stimulation it consistently reduced firing without altering firing in hilar neurons lacking YFP expression (Fig. 8*A–D*). Additionally, we verified that optical suppression of PV-INs did not induce persistent firing in GC or eliminate sustained firing in SGCs (Fig. 8*E*).

To directly test the contribution of PV-INs to esIPSC barrages in GCs and SGCs, we recorded esIPSCs in putative GC/SGC pairs in PV-NpHR3 mice in the absence or presence of amber light (2-s exposure starting 100 ms after the onset of PP stimulation; Fig. 9*A–C*). Light-on and light-off conditions were randomized (Fig. 9, trials with red lined in Fig. 9*D* indicate light-on first recordings). Surprisingly, esIPSC frequency in GCs, normalized to basal sIPSC frequency before stimulation, was not reduced by optical suppression of PV-INs (esIPSC frequency as % of prestimulus frequency, no-light: 264.59 ± 49.76, light: 225.85 ± 43.08, $N = 8$, $p > 0.05$, by paired t test; Fig. 9*D*). In contrast, recordings from SGCs showed a significant reduction in esIPSC frequency during suppression of PV-INs with amber-light (esIPSC frequency as % of prestimulus frequency, no-light: 209.76 ± 57.92, light: 127.86 ± 41.15, $N = 8$, $p = 0.015$ by paired t test; Fig. 8*D*). Thus, optical suppression of PV-INs selectively reduced esIPSC frequency in SGCs to approximately half of that observed in the absence of light demonstrating fundamental differences in inhibitory regulation of GCs and SGCs during evoked activity.

Discussion

Here, we identify that lateral sustained feedback inhibition, which has been proposed to shape dentate pattern separation and memory engram formation, is significantly lower in dentate SGCs than in GCs. We further show that PV-INs selectively support activity-driven sustained lateral inhibition of SGCs, but not GCs. The difference in local circuit feedback inhibitory

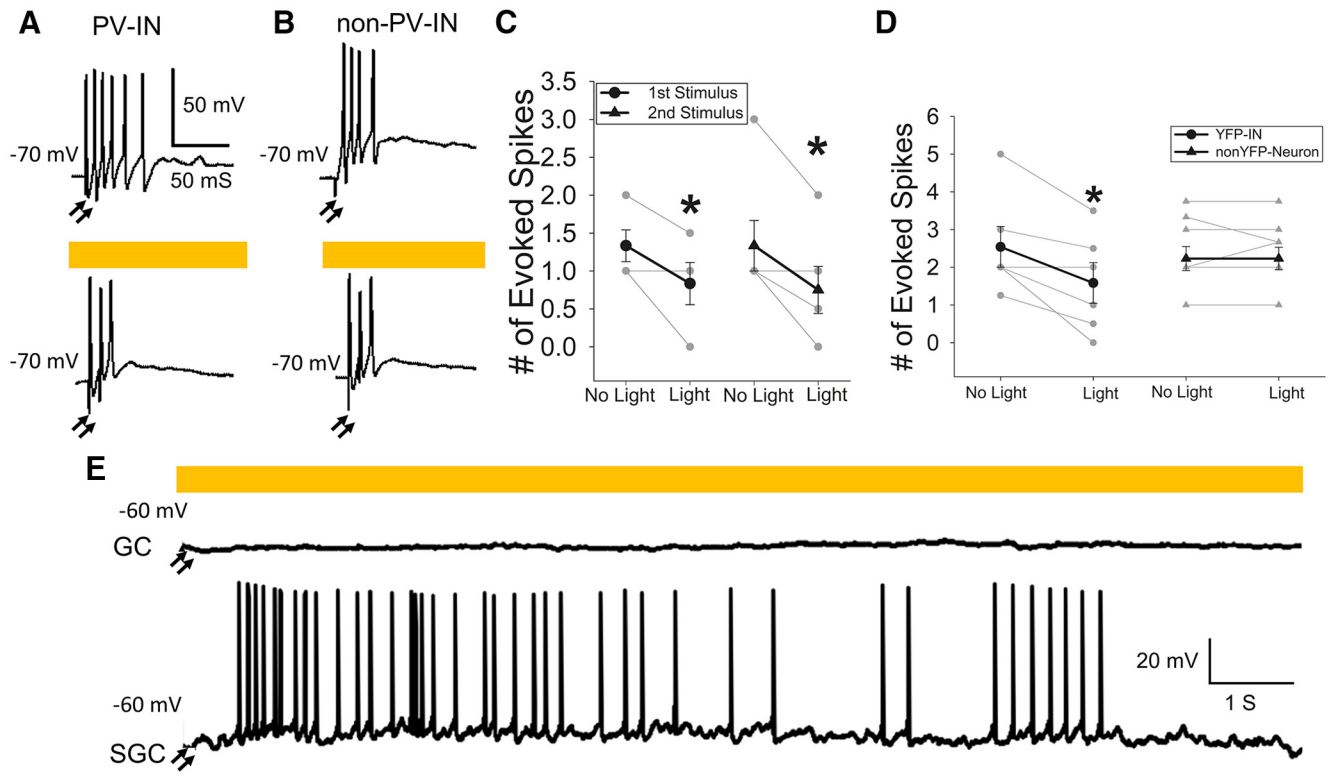

Figure 8. Cell specificity of halorhodopsin suppression of PV neuron firing. ***A***, Representative membrane voltage traces from a YFP-positive PV interneuron expressing halorhodopsin in the GC-hilar border in response to a pair of suprathreshold PP stimuli (denoted by two arrows) at 10-ms interval illustrated the early evoked firing in PV neurons (above). Effect of amber light exposure on PP evoked PV-IN firing is illustrated (below). ***B***, Example voltage traces from a YFP-negative hilar neuron in response to a pair of suprathreshold PP stimuli at 10-ms interval (above). Effect of amber light exposure on PP hilar neuron firing is illustrated (below). ***C***, Summary data of number of spikes elicited following the first and second stimuli and the effect of halorhodopsin activation on PP evoked firing in PV-IN. ***D***, Summary plot compares the effect of amber light on afferent evoke firing in halorhodopsin-expressing PV-IN and YFP-negative hilar neurons; $*p < 0.05$ by paired *t* test. Data presented as mean ± SEM. ***E***, Representative traces show lack of sustained firing in GCs and sustained firing in SGCs following paired suprathreshold PP stimulation. Text in gray box indicates recording condition.

regulation of SGCs and GCs during afferent activation could shape their distinct role in dentate processing.

SGCs, originally defined by Ramón y Cajal (1995) are a sparse, functionally distinct subpopulation of dentate output neurons with CA3 projections (Williams et al., 2007; Larimer and Strowbridge, 2010; Gupta et al., 2012; Save et al., 2018). Temporally structured inhibition by diverse interneurons projecting across the somato-dendritic axis help maintain the sparse GC activity needed for pattern separation (Arima-Yoshida et al., 2011; Dengler and Coulter, 2016; Hainmueller and Bartos, 2020). GCs receive distinct phases of synaptic inhibition including steady-state spontaneous synaptic inhibition, afferent evoked monosynaptic and disynaptic feedforward and feedback inhibition, as well as extrasynaptic inhibition (Soltesz et al., 1995; Kraushaar and Jonas, 2000; Stell et al., 2003). Additionally, afferent stimulation has been proposed to recruit sustained polysynaptic feedback GC inhibition (Larimer and Strowbridge, 2010). Focusing on synaptic inhibition, we demonstrate three functionally distinct phases of synaptic inhibition, namely, basal, early evoked, and sustained feedback synaptic inhibition in both GCs and SGCs and characterize the temporal profile and reliability of dentate evoked-sustained inhibition. We demonstrate that evoked-sustained feedback inhibition is not unique to GC but is present in SGCs as well. However, given the time-dependent changes in evoked-sustained inhibition and robust IPSC summation, we did not evaluate activity dependent changes in extrasynaptic GABA currents which are best examined in steady state. Although SGCs receive more frequent basal sIPSCs, GCs show greater enhancement of sustained feedback IPSCs on afferent activation. These data identify that compared with GCs, SGCs exhibit blunted elevation in inhibitory gating following input activation, which likely facilitates their ability to sustain prolonged firing in response to afferent activation.

Although GCs and SGCs differ in their development, structure, and excitability (Williams et al., 2007; Gupta et al., 2012, 2020; Save et al., 2018), neurochemical markers to distinguish the cell types are lacking and morphology, characterized in rats, is used as to classify SGCs and GCs. Whether the neuropeptide proenkephalin (PENK), expressed in some prox-1 positive dentate neurons tagged based on increases in the immediate early gene FOS (Erwin et al., 2020), is selective for SGCs remines to be determined. However, our clustering analysis based on morphometric parameters, and the PCA of underlying features validate the use of number of primary dendrites (>3), dendritic angle, and soma-aspect ratio to distinguish SGCs from GCs. Moreover, dendritic complexity, which could influence intrinsic physiology and input integration (Gulledge et al., 2005; van Elburg and van Ooyen, 2010; van der Velden et al., 2012), was significantly lower in SGCs than in GCs, as reported in rats (Gupta et al., 2020). Curiously, putative GCs segregated into two subclusters, based on dendritic complexity, dendritic angle, and number of primary dendrites raising the possibility that physiology of dentate projection neuron subtypes scales with number of primary dendrites and dendritic complexity. Nevertheless, the physiological differences between GCs and SGCs identified here and in earlier studies (Williams et al., 2007; Larimer and Strowbridge, 2010; Gupta et al., 2012; Save et al., 2018) justify examination of their role in the dentate circuit.

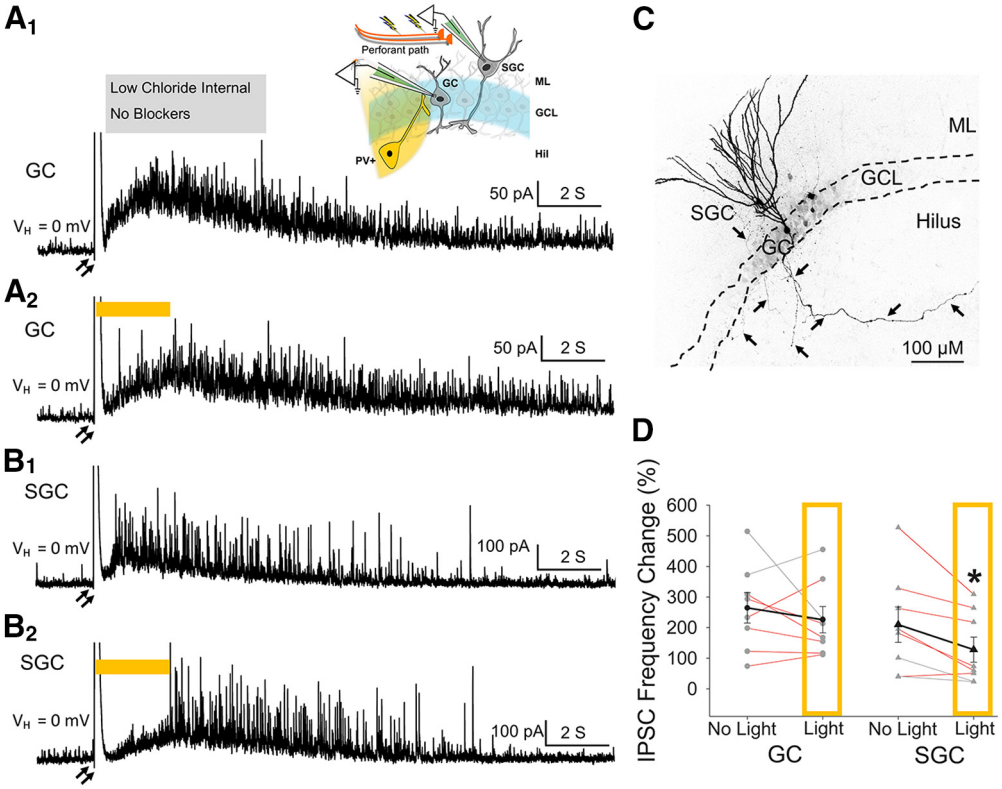

Figure 9. Optical suppression of PV-INs selectively reduces evoked sustained IPSCs in SGCs. ***A1***, Schematic illustrating the simultaneous dual GC-SGC recordings in response to paired stimulation of the PP and amber light stimulation (above). GC current trace illustrates the sustained increase in IPSC frequency compared with prestimulus baseline (below). ***A2***, GC trace shows that evoked sustained IPSCs in response to paired PP stimuli (denoted by two arrows) appears unchanged by amber light suppression (amber bar) of PV-INs. ***B1***, SGC current trace illustrates the sustained increase in IPSC frequency compared with prestimulus baseline. ***B2***, SGC trace shows that evoked sustained IPSCs in response to paired PP stimuli are suppressed by amber light. Note that the eIPSC peak is truncated to better illustrate the sustained change in IPSCs over 20 s. ***C***, Maximum intensity projection of a confocal image stack of a GC-SGC pair filled during recordings illustrated the soma location dendric arbors and hilar axon (arrows) of the cells. The image is presented as gray scale and inverted to better illustrate the axon. GCL, granule cell layer; ML, molecular layer; GC, granule cell; SGC, semilunar granule cell. ***D***, Summary plots of effect of amber light suppression of PV-INs on evoked sustained IPSC frequency in GCs and SGCs ($n = 8$ each). Red lines indicate trials with light-on first recordings. Data presented as mean ± SEM; $*p < 0.05$ by paired t test. Text in gray box indicates recording condition.

Consistent with prior findings in rats (Gupta et al., 2012, 2020), SGCs in mice receive more frequent sIPSCs than GCs. Since SGC somata and dendrites are located in the IML, outside the dense axonal arbor of PV-INs in the GCL, we anticipated fewer PV-INs inputs to SGCs than to GCs. Surprisingly, halorhodopsin suppression of PV-INs failed to reduce sIPSC frequency in both GCs and SGCs despite reliably hyperpolarizing (>5 mV) and reducing firing in YFP positive PV-INs. Moreover, channelrhodopsin activation of PV-INs evoked robust increases in GC and SGC IPSCs demonstrating viable, synaptically connected PV-INs. Furthermore, the same amber light protocol reduced evoked sustained IPSCs in SGCs, confirming the ability of halorhodopsin to suppress of PV-IN firing and synaptic release (Mahn et al., 2016). Why, then, is PV-IN suppression unable to reduce action potential dependent sIPSCs in GCs and SGCs even in the absence of glutamatergic blockers? One possibility is that PV-IN suppression disinhibits and increases firing of a subset of non-PV interneurons which compensate for the loss of PV-IN mediated inhibition. In this regard, the reciprocal activity states of PV and CCK neurons, recently reported in CA1, suggests that such a compensation is possible (Dudok et al., 2021). However, whether such a mechanism would exactly compensate for the reduction in PV-IN-mediated IPSCs in a slice is debatable and cannot be resolved by using chemogenetic strategies which would potentially suffer from similar network level changes. The inability of optical/chemogenetic silencing to disambiguate direct from circuit-effects need to be considered while using cell-specific silencing strategies (Bernard, 2020). Interestingly, a prior study found limited contribution of PV-INs to action potential independent miniature IPSCs in GCs (Goswami et al., 2012) and mutations impairing PV expression were shown to alter GC evoked IPSCs without impacting sIPSC frequency (Lucas et al., 2010). These findings are consistent with our results and raise the possibility that diverse populations of hilar and molecular layer interneurons may contribute substantively more than PV-INs to basal sIPSCs in GCs and SGCs. While our findings do not imply lack of PV-INs contribution to basal inhibition *in vivo*, the most parsimonious conclusion from our data are that PV-INs have limited role in basal sIPSCs in GCs and SGCs in slices.

PV-INs mediate robust and precise feedforward and feedback inhibition of GCs (Andersen et al., 1966; Hefft and Jonas, 2005; Ewell and Jones, 2010). We find that optical activation of PV-INs robustly increases IPSC frequency in both SGCs and GCs demonstrating that, despite their location in the IML, SGCs receive inhibitory synapses from PV-INs. Moreover, afferent evoked IPSC peak amplitude and kinetics of were not different between GCs and SGCs indicating that, unlike sIPSCs, inhibition evoked by a single PP stimulus is comparable between the cell types.

Finally, we examined sustained feedback inhibition, previously found to correlate with SGC firing and advanced as a mechanism for lateral inhibition (Larimer and Strowbridge,

2010). We confirm that paired suprathreshold PP stimulation elicits persistent SGC firing in ~50% of trials and was accompanied by a two-fold increase in IPSC frequency in both GCs and SGCs. Sustained SGC activity followed the early evoke firing by over 200 ms and persisted for over 10 s. Interestingly, although individual SGC firing was observed only in half the trials, GCs and/or SGCs showed evoked sustained IPSCs in all slices examined, suggesting that activation of a subset of SGCs may be sufficient to sustain feedback inhibition. We report that about half the PV-INs examined showed increased firing following paired PP stimulation with latency and duration corresponding to that of evoked sustained inhibition in GCs and SGCs. Notably, even PV-INs lacking sustained firing showed increased EPSP frequency following paired PP stimulation indicating enhanced glutamatergic drive. Since SGC axons selectively innervate PV-IN somata (Rovira-Esteban et al., 2020), our findings are consistent with sustained firing in SGCs, which does not occur in GCs, driving sustained PV-IN activity.

Although both SGCs and GCs show sustained increase in IPSCs following paired afferent stimulation, the relative increase in IPSC frequency in SGCs is significantly lower than in GCs. Thus, SGCs which receive more robust polysynaptic NMDA currents than GCs (Larimer and Strowbridge, 2010) are, yet, subject to less gating feedback synaptic inhibition placing them in a privileged position to support persistent firing. This enhanced firing likely promotes expression of activity-dependent genes and recruitment of SGCs as part of cellular ensembles during behavioral tasks (Erwin et al., 2020). Our analyses identify selective contribution of PV-INs to sustained feedback inhibition in SGCs but not in GCs. These results are paradoxical since wide field optical activation of PV-INs increases IPSCs in both SGCs and GCs and raises an intriguing possibility of target specific differences in PV-IN synaptic release and/or short-term plasticity similar to those reported in glutamatergic terminals (Sylwestrak and Ghosh, 2012; Blackman et al., 2013; Larsen and Sjöström, 2015; Éltes et al., 2017) or selective reciprocal connectivity between SGCs and a subset of PV-INs.

In conclusion, our study demonstrates an input strength dependent shift in three distinct temporal phases of synaptic inhibition between GCs and SGCs. During steady-state basal activity, SGCs receive greater synaptic inhibitory drive than GCs. In response to afferent activation, evoked synaptic inhibition in SGCs appears comparable to GCs, which, given the greater glutamatergic inputs reported in SGCs (Larimer and Strowbridge, 2010), represents a relative reduction in scaling of inhibition to excitation in SGCs. With further increase in drive during paired stimulation, the increase in sustained feedback inhibition in SGCs is lower than in GCs. This activity-dependent blunting of synaptic inhibitory inputs in SGCs compared with GCs indicates that SGCs, by having reduced activity-dependent inhibitory gating, may support a distinct role in dentate processing by integrating, rather than sparsifying, inputs and driving lateral inhibition and selectivity of GCs.

References

Alfonsa H, Merricks EM, Codadu NK, Cunningham MO, Deisseroth K, Racca C, Trevelyan AJ (2015) The contribution of raised intraneuronal chloride to epileptic network activity. J Neurosci 35:7715–7726.

Andersen P, Holmqvist B, Voorhoeve PE (1966) Entorhinal activation of dentate granule cells. Acta Physiol Scand 66:448–460.

Arima-Yoshida F, Watabe AM, Manabe T (2011) The mechanisms of the strong inhibitory modulation of long-term potentiation in the rat dentate gyrus. Eur J Neurosci 33:1637–1646.

Bekinschtein P, Kent BA, Oomen CA, Clemenson GD, Gage FH, Saksida LM, Bussey TJ (2013) BDNF in the dentate gyrus is required for consolidation of "pattern-separated" memories. Cell Rep 5:759–768.

Bernard C (2020) Optogenetics: keep interpretations light. eNeuro 7: ENEURO.0091-20.2020.

Blackman AV, Abrahamsson T, Costa RP, Lalanne T, Sjöström PJ (2013) Target-cell-specific short-term plasticity in local circuits. Front Synaptic Neurosci 5:11.

Braganza O, Mueller-Komorowska D, Kelly T, Beck H (2020) Quantitative properties of a feedback circuit predict frequency-dependent pattern separation. Elife 9:e53148.

Dengler CG, Coulter DA (2016) Normal and epilepsy-associated pathologic function of the dentate gyrus. Prog Brain Res 226:155–178.

Dudok B, Klein PM, Hwaun E, Lee BR, Yao Z, Fong O, Bowler JC, Terada S, Sparks FT, Szabo GG, Farrell JS, Berg J, Daigle TL, Tasic B, Dimidschstein J, Fishell G, Losonczy A, Zeng H, Soltesz I (2021) Alternating sources of perisomatic inhibition during behavior. Neuron 109:997–1012.e9.

Éltes T, Kirizs T, Nusser Z, Holderith N (2017) Target cell type-dependent differences in Ca(2+) channel function underlie distinct release probabilities at hippocampal glutamatergic terminals. J Neurosci 37:1910–1924.

Erwin SR, Sun W, Copeland M, Lindo S, Spruston N, Cembrowski MS (2020) A sparse, spatially biased subtype of mature granule cell dominates recruitment in hippocampal-associated behaviors. Cell Rep 31:107551.

Ewell LA, Jones MV (2010) Frequency-tuned distribution of inhibition in the dentate gyrus. J Neurosci 30:12597–12607.

Freund TF, Buzsáki G (1996) Interneurons of the hippocampus. Hippocampus 6:347–470.

GoodSmith D, Chen X, Wang C, Kim SH, Song H, Burgalossi A, Christian KM, Knierim JJ (2017) Spatial representations of granule cells and mossy cells of the dentate gyrus. Neuron 93:677–690.e5.

Goswami SP, Bucurenciu I, Jonas P (2012) Miniature IPSCs in hippocampal granule cells are triggered by voltage-gated Ca2+ channels via microdomain coupling. J Neurosci 32:14294–14304.

Gulledge AT, Kampa BM, Stuart GJ (2005) Synaptic integration in dendritic trees. J Neurobiol 64:75–90.

Gupta A, Elgammal FS, Proddutur A, Shah S, Santhakumar V (2012) Decrease in tonic inhibition contributes to increase in dentate semilunar granule cell excitability after brain injury. J Neurosci 32:2523–2537.

Gupta A, Proddutur A, Chang YJ, Raturi V, Guevarra J, Shah Y, Elgammal FS, Santhakumar V (2020) Dendritic morphology and inhibitory regulation distinguish dentate semilunar granule cells from granule cells through distinct stages of postnatal development. Brain Struct Funct 225:2841–2855.

Hainmueller T, Bartos M (2020) Dentate gyrus circuits for encoding, retrieval and discrimination of episodic memories. Nat Rev Neurosci 21:153–168.

Hefft S, Jonas P (2005) Asynchronous GABA release generates long-lasting inhibition at a hippocampal interneuron-principal neuron synapse. Nat Neurosci 8:1319–1328.

Hefft S, Kraushaar U, Geiger JR, Jonas P (2002) Presynaptic short-term depression is maintained during regulation of transmitter release at a GABAergic synapse in rat hippocampus. J Physiol 539:201–208.

Heinemann U, Beck H, Dreier JP, Ficker E, Stabel J, Zhang CL (1992) The dentate gyrus as a regulated gate for the propagation of epileptiform activity. Epilepsy Res Suppl 7:273–280.

Howard A, Tamas G, Soltesz I (2005) Lighting the chandelier: new vistas for axo-axonic cells. Trends Neurosci 28:310–316.

Husson F, Josse J, Pages J (2010) Principal component methods - hierarchical clustering - partitional clustering: why would we need to choose for visualizing data? Applied mathematics department, pp 1–17.

Korgaonkar AA, Li Y, Sekhar D, Subramanian D, Guevarra J, Swietek B, Pallottie A, Singh S, Kella K, Elkabes S, Santhakumar V (2020) Toll-like receptor 4 signaling in neurons enhances calcium-permeable α-amino-3-hydroxy-5-methyl-4-isoxazolepropionic acid receptor currents and drives post-traumatic epileptogenesis. Ann Neurol 87:497–515.

Kraushaar U, Jonas P (2000) Efficacy and stability of quantal GABA release at a hippocampal interneuron-principal neuron synapse. J Neurosci 20:5594–5607.

Larimer P, Strowbridge BW (2010) Representing information in cell assemblies: persistent activity mediated by semilunar granule cells. Nat Neurosci 13:213–222.

Larsen RS, Sjöström PJ (2015) Synapse-type-specific plasticity in local circuits. Curr Opin Neurobiol 35:127–135.

Lothman EW, Stringer JL, Bertram EH (1992) The dentate gyrus as a control point for seizures in the hippocampus and beyond. Epilepsy Res Suppl 7:301–313.

Lucas EK, Markwardt SJ, Gupta S, Meador-Woodruff JH, Lin JD, Overstreet-Wadiche L, Cowell RM (2010) Parvalbumin deficiency and GABAergic dysfunction in mice lacking PGC-1alpha. J Neurosci 30:7227–7235.

Mahn M, Prigge M, Ron S, Levy R, Yizhar O (2016) Biophysical constraints of optogenetic inhibition at presynaptic terminals. Nat Neurosci 19:554–556.

Otis TS, Staley KJ, Mody I (1991) Perpetual inhibitory activity in mammalian brain slices generated by spontaneous GABA release. Brain Res 545:142–150.

Ramón y Cajal S (1995) Histology of the nervous system of man and vertebrates. New York: Oxford University Press.

Rovira-Esteban L, Hájos N, Nagy GA, Crespo C, Nacher J, Varea E, Blasco-Ibáñez JM (2020) Semilunar granule cells are the primary source of the perisomatic excitatory innervation onto parvalbumin-expressing interneurons in the dentate gyrus. eNeuro 7:ENEURO.0323-19.2020.

Santhakumar V (2008) Modeling mossy cell loss and mossy fiber sprouting in epilepsy. In: Computational neuroscience in epilepsy (Soltesz I, Staley KJ, eds), pp 89–111. San Diego: Academic Press.

Save L, Baude A, Cossart R (2018) Temporal embryonic origin critically determines cellular physiology in the dentate gyrus. Cereb Cortex 29:2639–2652.

Sik A, Penttonen M, Buzsáki G (1997) Interneurons in the hippocampal dentate gyrus: an in vivo intracellular study. Eur J Neurosci 9:573–588.

Soltesz I, Smetters DK, Mody I (1995) Tonic inhibition originates from synapses close to the soma. Neuron 14:1273–1283.

Stell BM, Brickley SG, Tang CY, Farrant M, Mody I (2003) Neuroactive steroids reduce neuronal excitability by selectively enhancing tonic inhibition mediated by delta subunit-containing GABAA receptors. Proc Natl Acad Sci USA 100:14439–14444.

Sylwestrak EL, Ghosh A (2012) Elfn1 regulates target-specific release probability at CA1-interneuron synapses. Science 338:536–540.

van der Velden L, van Hooft JA, Chameau P (2012) Altered dendritic complexity affects firing properties of cortical layer 2/3 pyramidal neurons in mice lacking the 5-HT3A receptor. J Neurophysiol 108:1521–1528.

van Elburg RA, van Ooyen A (2010) Impact of dendritic size and dendritic topology on burst firing in pyramidal cells. PLoS Comput Biol 6: e1000781.

Walker MC, Pavlov I, Kullmann DM (2010) A 'sustain pedal' in the hippocampus? Nat Neurosci 13:146–148.

Williams PA, Larimer P, Gao Y, Strowbridge BW (2007) Semilunar granule cells: glutamatergic neurons in the rat dentate gyrus with axon collaterals in the inner molecular layer. J Neurosci 27:13756–13761.

Yu J, Swietek B, Proddutur A, Santhakumar V (2015) Dentate total molecular layer interneurons mediate cannabinoid-sensitive inhibition. Hippocampus 25:884–889.

Yu J, Proddutur A, Swietek B, Elgammal FS, Santhakumar V (2016) Functional reduction in cannabinoid-sensitive heterotypic inhibition of dentate basket cells in epilepsy: impact on network rhythms. Cereb Cortex 26:4229–4314.